Direct Formation of Thermally Stabilized Amorphous Mesoporous Fe₂O₃/SiO₂ Nanocomposites by Hydrolysis of Aqueous Iron (III) Nitrate in Sols of Spherical Silica Particles

Kamal M.S. Khalil,* Hatem A. Mahmoud, and Tarek T. Ali

Chemistry Department, Faculty of Science, Sohag University, P.O. Box 82524, Sohag, Egypt

Nanocomposite materials containing 10% and 20% iron oxide/silica, Fe₂O₃/SiO₂ (w/w), were prepared by direct hydrolysis of aqueous iron (III) nitrate solution in sols of freshly prepared spherical silica particles (Stöber particles) present in their mother liquors. This was followed by aging, drying, calcination up to 600 °C through two different ramp rates, and then isothermal calcinations at 600 °C for 3 h. The calcined and the uncalcined (dried at 120 °C) composites were characterized by thermogravimetric analysis, differential scanning calorimetry, Fourier transform infrared spectroscopy, X-ray diffraction (XRD), N₂ adsorption/desorption techniques, and scanning electron microscopy as required. XRD patterns of the calcined composites showed no line broadening at any *d*-spacing positions of iron oxide phases, thereby reflecting the amorphous nature of Fe₂O₃ in the composite. The calcined composites showed nitrogen adsorption isotherms characterizing type IV isotherms with high surface area. Moreover, surface area increased with the increasing of the iron oxide ratio and lowering of the calcination ramp rate. Results indicated that iron oxide particles were dispersed on the exterior of silica particles as isolated and/or aggregated nanoparticles. The formation of the title composite was discussed in terms of the hydrolysis and condensation mechanisms of the inorganic Fe(III) precursor in the silica sols. Thereby, fast nucleation and limited growth of hydrous iron oxide led to the formation of nanoparticles that spread interactively on the hydroxylated surface of spherical silica particles. Therefore, a nanostructured composite of amorphous nanoparticles of iron oxide (as a shell) spreading on the surface of silica particles (as a core) was formed. This morphology limited the aggregation of Fe₂O₃ nanoparticles, prevented silica particle coalescence at high temperatures, and enhanced thermal stability.

1. Introduction

Nanocomposite iron oxide/silica (Fe₂O₃/SiO₂) materials have been found to exhibit interesting physicochemical properties suitable for many advanced nanotechnological applications as catalysts,[1,2] adsorbents for metal removal,[3] porous adsorbents for the isolation of genomic DNA,[4] humidity sensors,[5] magnetic colloidal particles,[6] magnetic-optical materials,[7] platforms for the growth of carbon nanotubes,[8] and many other applications.

Several strategies have recently been reported for the synthesis of Fe₂O₃/SiO₂ nanocomposites. Thus, iron oxide nanoparticles were synthesized within mesoporous MCM-48 silica phases[9] by using multiple cycles of wet impregnation, drying, and calcination procedures. Nanoparticles of iron oxide were deposited on the exterior of and inside the pores of hexagonal mesoporous silica by a direct synthesis technique with iron phthalocyanine as a precursor.[8] Composites that consisted of γ-Fe₂O₃ nanocrystals (4−10 nm) dispersed in submicrometer spherical silica particles

were prepared by aerosol pyrolysis of a methanol solution containing tetraethoxysilane (TEOS) and iron nitrate.[6] FeₓOᵧ−SiO₂ nanocomposites were prepared by the sol−gel method using two different SiO₂ sources—TEOS and methyltriethoxysilane (MTEOS)—and FeSO₄·7H₂O.[10]

However, the sol−gel process has been proven to be a successful preparative route for Fe₂O₃/SiO₂ nanocomposites.[1,7−19] Thus, for the iron oxide phase, quite a lot of precursors have been implemented, which included many inorganic precursors such as FeSO₄·7H₂O,[10,11] FeCl₂·4H₂O,[12] FeCl₃·6H₂O,[13] and most frequently Fe (NO₃)₃·9H₂O.[1,5−7] Moreover, a number of metallorganic sources such as iron methoxyethoxide, Fe(OC₂H₄-OCH₃)₃,[5] Fe(OC₂H₅)₃,[14] iron(III) acetylacetonate,[15] iron phthalocyanine,[8] or iron pentacarbonyl (Fe(CO)₅)[16] were also examined. In contrast, for the SiO₂ source, fewer alkoxides were employed, such as tetramethoxysilane (TMOS),[8] MTEOS,[10] or most frequently TEOS.[1,7,9,10,16−19] Finally, to accomplish the formation of Fe₂O₃/SiO₂ materials, a thermal treatment of the resulted dry gel at higher temperatures, typically ≥200 °C, should be conducted.[13]

* Corresponding author. Phone: +20 121 138 223; fax: +20 934 601 159; e-mail: kamal.khalil@sci.sohag.edu.eg.

(1) Szegedi, A.; Konya, Z.; Mehn, D.; Solymar, E.; Pal-Borbely, G.; Horvath, Z. E.; Biro, L. P.; Kiricsi, I. *Appl. Catal. A: Gen.* **2004**, *272*, 257.

(2) Bachari, K.; Millet, J. M. M.; Bonville, P.; Cherifia, O.; Figueras, F. *J. Catal.* **2007**, *249*, 52.

(3) Unob, F.; Wongsiri, B.; Phaeon, N.; Puanngam, M.; Shiowatana, J.; *J. Hazard. Mater.* **2007**, *142*, 455.

(4) Zhang, Z.; Zhang, L.; Chen, L.; Chen, L.; Wan, Q-H. *Biotechnol. Prog.* **2006**, *22*, 514.

(5) Tongpool, R.; Jindasuwan, S. *Sens. Actuators, B* **2005**, *106*, 523.

(6) Tartaj, P.; Gonzalez-Carreno, T.; Serna, C. J. *J. Phys. Chem. B* **2003**, *107*, 20.

(7) Moreno, E. M.; Zayat, M.; Morales, M. P.; Serna, C. J.; Roig, A.; Levy, D. *Langmuir* **2002**, *18*, 4972.

(8) Barreca, D.; Blau, W. J.; Croke, G. M.; Deeney, F. A.; Dillon, F. C.; Holmes, J. D.; Kufazvinei, C.; Morris, M. A.; Spalding, T. R.; Tondello, E. *Microporous Mesoporous Mater.* **2007**, *103*, 142.

(9) Froba, M.; Kohn, R.; Bouffaud, G.; Richard, O.; van Tendeloo, G. *Chem. Mater.* **1999**, *11*, 2858.

(10) Predoi, D., Crisan, O.; Jitianu, A.; Valsangiacom, M. C.; Raileanu, M.; Crisan, M.; Zaharescu, M. *Thin Solid Films* **2007**, *515*, 6319.

(11) Chaneac, C.; Tronc, E.; Jolivet, J. P. *Mater. Chem.* **1996**, *6*, 1905.

(12) Zaharescu, M.; Crisan, M.; Jitianu, A.; Crisan, D.; Meghia, A.; Rau, I. *J. Sol-Gel Sci. Technol.* **2000**, *19*, 631.

(13) Clapsaddle, B. J.; Gash, A. E.; Satcher, J. H., Jr.; Simpson, R. L. *J. Non-Cryst. Solids* **2003**, *331*, 190.

(14) Guglielmi, M.; Principi, G. *J. Non-Cryst. Solids* **1982**, *48*, 161.

(15) Tanaka, K.; Kamiya, K.; Matsuoka, M.; Yoko, T. *J. Non-Cryst. Solids* **1987**, *94*, 356.

(16) Ramesh, S.; Prozorov, R.; Gedanken, A. *Chem. Mater.* **1997**, *9*, 2996.

(17) del Monte, F.; Morales, M. P.; Levy, D.; Fernandez, A.; Ocana, M.; Roig, A.; Molins, E.; O'Grady, K.; Serna, C. J. *Langmuir* **1997**, *13*, 3627.

(18) Ennas, G.; Musinu, A.; Piccaluga, G.; Zedda, D.; Gatteschi, D.; Sangregorio, C.; Stanger, J. L.; Concas, G.; Spano, G. *Chem. Mater.* **1998**, *10*, 495.

(19) Solinas, S.; Piccaluga, G.; Morales, M. P.; Serna, C. J. *Acta Mater.* **2001**, *49*, 2805.

However, on the basis of the precursor types and the temperature at which the resultant dried gels were calcined, the formation of *amorphous*, α-, or γ-Fe_2O_3/SiO_2 composites have been reported.[2-7,16-19] In spite of the large number of publications dealing with the preparation of α-Fe_2O_3/SiO_2,[2,4,5,10] and γ-Fe_2O_3/SiO_2[6,7,17-19] composites, fewer articles have dealt with the preparation of amorphous Fe_2O_3/SiO_2,[16,18] composites. Amorphous Fe_2O_3 on its own has captured growing interest as an advanced type of material.[20] This was because amorphous Fe_2O_3 nanoparticles are more active than the nanocrystalline polymorphs or particles of metallic iron of the same diameter.[21] However, to utilize such an amorphous form efficiently in catalytic and/or membrane applications, it is important to stabilize it thermally. Thus, the amorphous nature, high surface area, and mesoporosity are preserved during utilization at high temperatures.

Recently, Khalil et al. have employed a successful approach for the preparation of thermally stable TiO_2/SiO_2[22] and CeO_2/SiO_2[23] nanocomposite materials, which involved freshly prepared colloidal spherical silica particles known as Stöber particles.[24] In fact, a large variety of nanostructured materials have been made based on the Stöber silica particles.[25-29] This stems from the advantages of the well-known surface chemistry of silica, which permits its modification with different functional groups[25,26] and also the chemical binding of metal oxide nanoparticles.[16,22,23,27-29] This modification produces more stable particles and/or composites of modified and interesting properties. In the present work, we investigate the formation of 10 and 20% (w/w) FeO_3/SiO_2 composites via a direct method. This method involves the hydrolysis of $Fe(NO_3)_3 \cdot 9H_2O$ in the mother liquor of a freshly prepared Stöber silica sol, which is followed by aging, drying, and calcination at 600 °C for 3 h. The texture and structure of the produced composite materials are characterized by the appropriate techniques.

2. Experimental

2.1. Materials. Iron(III) nitrate nonahydrate [$Fe(NO_3)_3 \cdot 9H_2O$ (assayed), 98% (+), solid product of Prolabo, France], tetraethyl orthosilicate [$Si(OC_2H_5)_4$ (TEOS), 98%, liquid product of Sigma—Aldrich Company, Ltd., Germany], ethyl alcohol [C_2H_5OH, 99.5%, product of Adwic, Egypt], and aqueous ammonia solution [25% NH_3, 99.99%, product of BDH, Ltd., England] were purchased and used as received.

2.1.1. Preparation of the Blank Silica Material. The blank silica material was prepared by the Stöber method.[24] Details of the preparation method are given elsewhere.[22-24] In brief, a 19.0 mL volume of TEOS was added to 207.0 mL of absolute alcohol, and hydrolysis was initiated by the addition of 155 mL of ammonia (within 1 min) with magnetic stirring (400 rpm), resulting in the formation of Stöber silica sol. The sol was maintained under continuous stirring for 1 h. The produced material was filtered off and dried at 120 °C for 24 h. The resultant material is termed

uncalcined blank silica. The R1 (see below for details) calcination product is termed *calcined blank silica.*

2.1.2. Preparation of Fe_2O_3/SiO_2 Composites. Composites containing 10 and 20% Fe_2O_3/SiO_2 (w/w) were prepared as follows. A calculated amount of $Fe(NO_3)_3 \cdot 9H_2O$ corresponding to 10 or 20% Fe_2O_3/SiO_2 (w/w) was dissolved in 50 mL of doubly distilled water. The resultant solution was transferred into a beaker containing freshly prepared Stöber silica sol prepared by the method described above. The solution was magnetically stirred at ca. 400 rpm and was maintained under constant stirring for 1 h. The resultant solution was aged for 7 days at room temperature (RT). The precipitate thus obtained was filtered off and then dried for 24 h at 60 °C, followed by further drying at 120 °C for 24 h. The resultant materials are termed *uncalcined 10%* and *20% Fe_2O_3/SiO_2 composites*, respectively. Portions of the uncalcined materials obtained by this method were calcined by two different ramp rates, namely, 1 and 10 °C min⁻¹ up to the target calcination temperature (600 °C) and kept isothermally at this temperature for 3 h. Calcined materials were named after their respective precursors as *calcined 10%* and *20% Fe_2O_3/SiO_2 composites*. Composites obtained by calcinations at ramp rates of 1 and 10 °C min⁻¹, respectively, are designated by the suffix *R1* and *R10*, i.e., Fe_2O_3/SiO_2 (R1) and Fe_2O_3/SiO_2 (R10).

2.2. Characterization. *2.2.1. Thermal Analyses (Thermogravimetric Analysis (TGA) and Differential Scanning Calorimetry (DSC)).* Analyses were carried out utilizing a Thermal Analyst 2000 TA instrument (U.S.A.) controlling a 2050 thermogravimetric analyzer and a 2010 differential scanning calorimeter (DSC). A platinum ceramic sample boat was used for TGA analysis. Samples weighing 10.0 ± 0.1 mg were heated up to 600 °C at 10 °C min⁻¹, in a flow (40 mL/min) of nitrogen (N_2) or oxygen (O_2) atmosphere. For the DSC measurements, aluminum open pans (without lids) were used to allow interaction of the sample with the DSC cell atmosphere, according to the instructions given in the operator's manual of the above indicated analyzer. Samples weighing 5.0 ± 0.1 mg were heated up to 500 °C at 10 °C min⁻¹, in a flow (40 mL/min) of N_2 or O_2 atmosphere, as indicated.

2.2.2. Fourier Transform Infrared (FTIR) Spectroscopy. FTIR spectra of the KBr-supported test samples were obtained by using an FTIR spectrophotometer (Nicolet FTIR Magna-IR 560 system, U.S.A.), in the range 4000—400 cm⁻¹, with 40 scans and a resolution of 4 cm⁻¹.

2.2.3. X-ray Diffraction (XRD). XRD patterns were obtained using a Philips 1840 diffractometer at RT. Diffraction patterns were obtained with Ni-filtered Cu K_α radiation ($\lambda = 0.154056$ nm). The patterns obtained were matched with the standard data[30] for the purpose of phase identification.

2.2.4. Nitrogen Gas Adsorption. Nitrogen adsorption/desorption isotherms at −196 °C were measured using a model ASAP 2010 instrument (Micromeritics Instrument Corporation, U.S.A.). Prior to measurement, each sample was degassed for 2 h at 250 °C to 0.1 Pa. The specific surface area, S_{BET}, was calculated by applying the Brunauer—Emmett—Teller (BET) equation.[31] The average pore diameter was estimated from the relation $4V_pS_{BET}^{-1}$, where V_p is the total pore volume (at $pp_o^{-1} = 0.975$). Pore width distribution over the mesopore range was generated by the Barrett—Joyner—Halenda (BJH)[32] analysis of the adsorption branches, and values of the average pore width were calculated. Microporosity was assessed from the t-plot method,[33] using Harkins—Jura correlation[34] for a t-plot as a function of the normalized pressure, pp_o^{-1}. Surface areas obtained by the t-plot method, S_t, were calculated from slope analysis of the t-plots. Micropore surface area, S_{mic}, the area corresponding to the gas condensed in micropores, was calculated from the relation $S_{mic} = S_{BET} - S_t$.

(20) Machala, L.; Zboril, R.; Gedank, A. *J. Phys. Chem. B* **2007**, *111*, 4003.

(21) Srivastava, D. N.; Perkas, N.; Gedanken, A.; Felner, I. *J. Phys. Chem. B* **2002**, *106*, 1878.

(22) Khalil, K. M. S.; Elsamahy, A. A.; Elanany, M. S. *J. Colloid Interface Sci.* **2002**, *249*, 359.

(23) Khalil, K. M. S.; Elkabee, L. A.; Murphy, B. *J. Colloid Interface Sci.* **2005**, *287*, 534.

(24) Stöber, W.; Fink, A.; Bohn, E. *J. Colloid Interface Sci.* **1968**, *26*, 62.

(25) Lee, M. H.; Beyer, F. L.; Furst, E. M. *J. Colloid Interface Sci.* **2005**, *288*, 114.

(26) Choi, H.; Chen, I.-W. *J. Colloid Interface Sci.* **2003**, *258*, 435.

(27) Wang, H.; Chen, Y.; Nakamura, H.; Yao, K.; Nishimura, S.; Abe, E. *Chem. Lett.* **2002**, *6*, 630.

(28) Im, S. H.; Herricks, T.; Lee, Y. T.; Xia, Y. *Chem. Phys. Lett.* **2005**, *401*, 19.

(29) Söderberg, O.; Ge, Y.; Haimi, E.; Heczko, O.; Oja, M.; Laine, J.; Suhonen, T.; Aaltonen, A.; Kalliokari, K.; Borak, B.; Jasiorski, M.; Baszczuk, A.; Maruszewski, K.; Hannula, S.-P. *Mater. Lett.* **2007**, *61*, 3171.

(30) JCPDS—International Centre for Diffraction Data, CD, 1996.

(31) Brunauer, B.; Emmett, P. H.; Teller, E. *J. Am. Chem. Soc.* **1938**, *60*, 309.

(32) Barrett, E. P.; Joyner, L. G.; Halenda, P. H. *J. Am. Chem. Soc.* **1951**, *73*, 373.

(33) Webb, P. A.; Orr, C. *Analytical Method in Fine Particle Technology*; Micrometrics: Norcross, GA, 1997.

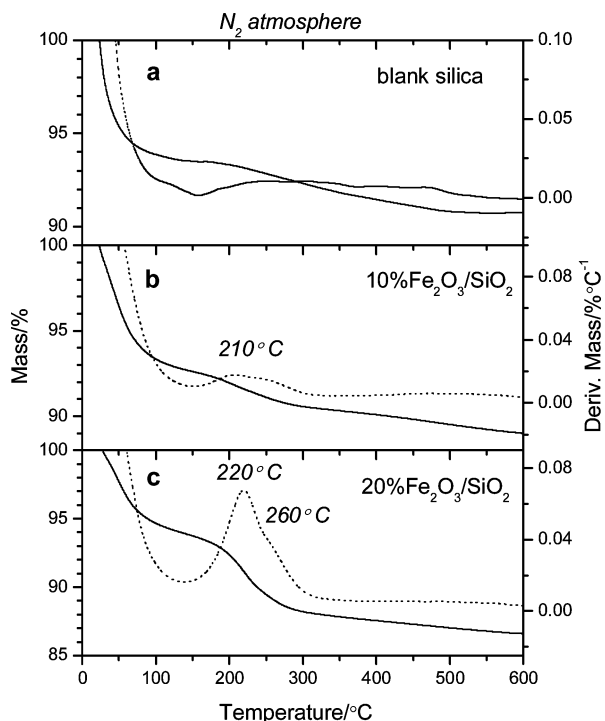(34) Harkins, W. D.; Jura, G. J. *J. Chem. Phys.* **1943**, *11*, 431.

Figure 1. TGA and DTG curves for the uncalcined (a) blank silica, (b) 10% Fe$_2$O$_3$/SiO$_2$, and (c) 20% Fe$_2$O$_3$/SiO$_2$ materials in a flow of N$_2$ atmosphere.

Figure 2. TGA and DTG curves for the uncalcined (a) blank silica, (b) 10% Fe$_2$O$_3$/SiO$_2$, and (c) 20% Fe$_2$O$_3$/SiO$_2$ materials in a flow of O$_2$ atmosphere.

2.2.5. Scanning Electron Microscopy (SEM). SEM micrographs were obtained using a Jeol microscope, model JSM-5600. Samples were coated with gold before investigation.

3. Results and Discussion

3.1. Thermal (TGA and DSC) Analyses. TGA and derivative thermogravimetry (DTG) curves for the uncalcined materials in the flow of N$_2$ atmosphere are shown in Figure 1. The obtained results are summarized in Table 1. TGA curves for the uncalcined blank silica as well as for the composite materials showed a case of continuous mass loss against temperature. However, a stable mass region at 520−600 °C was observed for the blank silica, but mass loss extended over the full test range for the composite materials. The corresponding TGA and DTG curves for the uncalcined materials in a flow of O$_2$ atmosphere are shown in Figure 2. Instead of the continuous mass loss observed for the composites in a flow of N$_2$, a case of stable mass was observed for the 10% composite precursor at 560−600 °C. Even more, a very small mass gain, above 420 °C, was observed for the 20% composite precursor material. This may be due to the formation of lower FeO$_x$ species (below 420 °C) as an intermediate during the formation process of Fe$_2$O$_3$. Mass loss values recorded over the range of RT up to 600 °C were 9.3, 11.0, and 13.4% in the flow of N$_2$ atmosphere (or 11.1, 9.6, and 11.2% in the flow of oxygen atmosphere), respectively, for the uncalcined blank silica, 10%, and 20% composite materials. This indicates that more mass loss occurred in N$_2$ than in O$_2$ atmosphere, which is probably
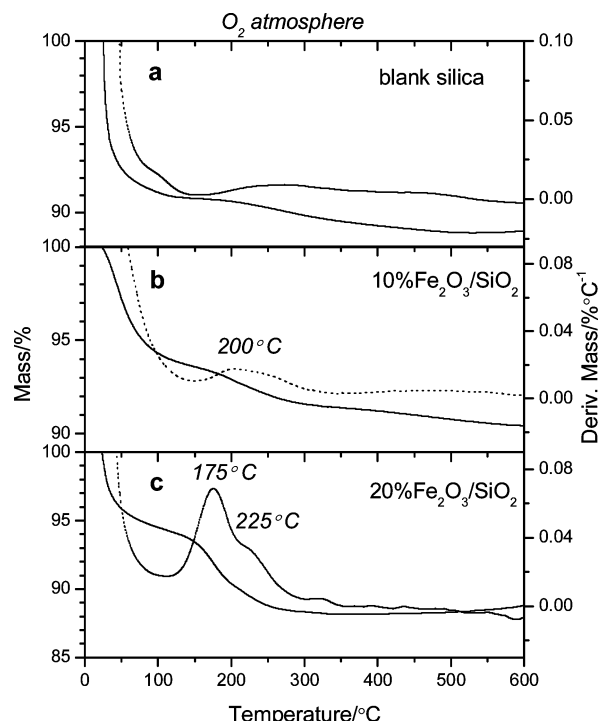
due to the partial reduction of iron oxide species in the N$_2$ atmosphere and full oxidation of these species in flow of O$_2$ atmosphere. However, the major part of the indicated mass loss in flow of either N$_2$ or O$_2$ atmosphere occurred below 350 °C for the different sample, and very small mass change occurred above this temperature, as shown in Table 1.

The DTG curve for the pure silica showed no recognizable peaks in a flow of either N$_2$ or O$_2$ atmosphere, as shown in Figures 1 and 2, respectively. However, for the uncalcined 10% composite, a peak was observed at 210 °C in the flow of N$_2$ atmosphere (or at 200 °C in the flow of O$_2$ atmosphere). A similar DTG peak, however larger, was observed for the uncalcined 20% composite at 220 °C (N$_2$) or 175 °C (O$_2$). The latter peak for the 20% was accompanied by a weak shoulder at 260 °C (N$_2$) or 225 °C (O$_2$), as shown respectively in Figures 1 and 2. It is known that TGA for the pure silica precursor in nitrogen atmosphere originates mainly from desorption of physically adsorbed water (and/or solvents) and surface dehydroxylation of the silica surfaces.[22,23] Thus, it is reasonable to suggest association of the newly developed peak (and its shoulder) for the decomposition processes of the precursor species of iron oxide.

DSC curves for the uncalcined test materials, carried out in a flow of N$_2$ or O$_2$ atmosphere, are shown in Figure 3 (top and bottom, respectively). In the flow of N$_2$ atmosphere, the uncalcined blank silica and the composite materials showed one main endothermic peak over the range of RT to 200 °C. However, the

Table 1. Summary of the TGA Results for the Uncalcined Composite Materials in Flow of N$_2$ or O$_2$ Atmosphere[a]

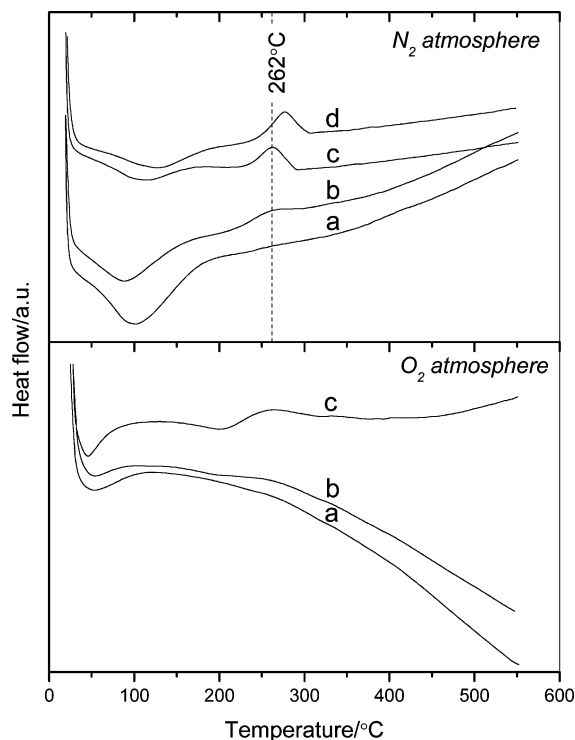|	N$_2$ atmosphere				O$_2$ atmosphere			
	mass loss at				mass loss at			
material	350°C	600°C	DTG peaks	DSC peaks	350°C	600°C	DTG peaks	DSC peaks
pure SiO$_2$	8.2	9.3		<120 °C	10.5	11.1		
10% Fe$_2$O$_3$/SiO$_2$	9.7	11.0	210°C	<120 °C end, 275 °C ex	8.6	9.6	200 °C	<120 °C end, ~ 200 °C end
20% Fe$_2$O$_3$/SiO$_2$	12.2	13.4	220°C, 260 °C Sh	<120 °C end, 275 °C ex	11.8	11.2	175 °C, 220 °C Sh	<120 °C end, 200 °C end

[a] Sh = shoulder, end = endothermic, ex = exothermic.

Figure 3. DSC curves in a flow of N_2 atmosphere (top) or O_2 atmosphere (bottom) for the uncalcined (a) blank silica, (b) 10% Fe_2O_3/SiO_2, and (c) 20% Fe_2O_3/SiO_2 materials carried out at 10 °C min^{-1}; (d) DSC curves for the uncalcined 20% Fe_2O_3/SiO_2 carried out at 20 °C min^{-1} in flow of N_2 atmosphere.

uncalcined composites showed an additional exothermic peak in the region of 230–310 °C (maximum at 262 °C), which was not observed for the uncalcined blank silica. This peak was found to move further (to 277 °C) when the DSC measurement was carried out at a higher ramp rate (20 °C min^{-1}) under the same atmosphere (N_2). However, when DSC measurements were carried out in a flow of O_2 atmosphere (at 10 °C min^{-1}), as shown in Figure 3 (bottom), the above-mentioned exothermic peak was completely or substantially smeared, respectively, for the uncalcined 10% and 20% composites. Moreover, for the latter composite, another endothermic peak was observed at $\sim$220 °C. Dependence of the exothermic peak on the type of atmosphere suggests its association with the decomposition and/ or combustion of some adsorbed species that associated with the presence of the iron oxide precursor.

However, crystallization of pure amorphous iron oxide nanoparticles was recently reported[20] where an exothermic DSC peak was observed at $\sim$280 °C in the flow of N_2 atmosphere, which was ascribed to the transformation of Fe_2O_3 from amorphous into gamma phase, or associated with the loss of organic species and magnetite formation (γ-Fe_2O_3).[35] Clear evidence for the association of this exothermic peak with the process of amorphous to γ-Fe_2O_3 nanoparticle transformation in a silica matrix was obtained by comparison of differential thermal analysis data for the initial gel and the data obtained after it was washed with water.[17] However, the important difference between both gels was observed at temperatures greater than 200 °C, where an exothermic peak, associated with the loss of organic species and magnetite formation, disappeared completely when the gel was washed. XRD analysis of the samples after heating at 400 °C gives only γ-Fe_2O_3 in the first case, whereas the washed sample results in a completely amorphous material.[17]
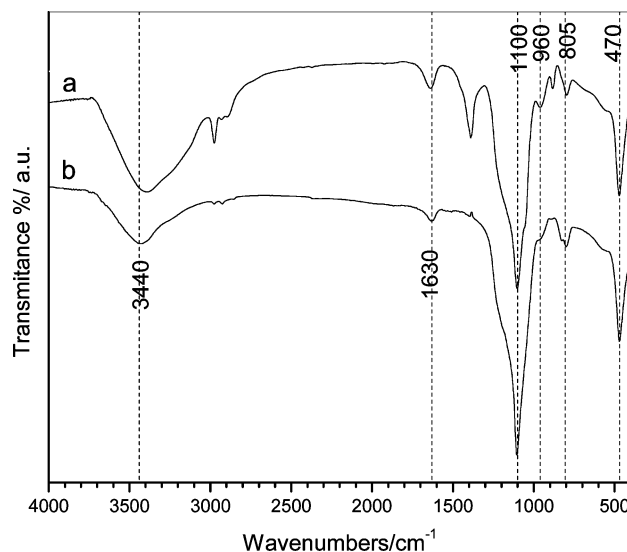
(35) do Carmo Rangel, M.; Galembeck, F. *J. Catal.* **1994**, *145*, 3647.

Figure 4. FTIR spectra for the (a) uncalcined 20% Fe_2O_3/SiO_2, and (b) calcined 20% Fe_2O_3/SiO_2 R10 composites.

Therefore, it could be concluded that retardation for the amorphous phase transformation to the gamma phase occurs upon calcination of nano iron particles in a flow of O_2 (or air) atmosphere. The above discussion is further supported by the FTIR and XRD results, as shown below.

3.2. FTIR Spectra. FTIR spectra for the uncalcined 20% Fe_2O_3/SiO_2 composite, as a representative of the uncalcined materials, is shown in Figure 4, spectrum a. The spectrum for the uncalcined 20% composite exhibits a group of bands that agree with the band positions reported for silica gel.[22,23] Typically, bands were observed as follows: the band at 3440 cm^{-1} corresponds to the ν(O–H) mode of (H-bonded) water molecules; the band at 1630 cm^{-1} corresponds to the δ(OH) mode; the band at 960 cm^{-1} corresponds to ν(Si–OH); the bands at 1100 and 805 cm^{-1} correspond to ν_{as}(Si–O–Si) and ν_s(Si–O–Si) modes, respectively; and the band at 470 cm^{-1} corresponds to the δ-(Si–O–Si) mode. In addition to the above group of bands, the spectrum for the uncalcined 20% composite evidently showed a few more bands. These bands appear at $\sim$3200 cm^{-1}, which may be assigned to adsorbed ammonia species from the preparation media, at $\sim$1400 cm^{-1} (maximum at 1385 cm^{-1}), which may be due to adsorbed ammonia and/or nitrate species, and a few small bands below 3000 cm^{-1}, which may be assigned to the presence of adsorbed alcoholic species. It was found that the latter group of bands, associated with the indicated adsorbed species from the preparation media, was more intense for the spectrum of 20% composite than for the spectrum of 10% composite (not shown). This suggests that the latter group of bands were related to the presence of more Fe_2O_3 precursor species. These results are in agreement with the above thermal analyses results. Moreover, a very small band shoulder at 595 cm^{-1} was also developed, which is assignable to ν Fe–O in Fe–O–Fe systems.[10]

However, spectra of the different calcined materials only showed the group of bands that are characteristic for silica gel; no bands for the adsorbed species remained. This indicates that all of the adsorbed species were removed during the calcination processes. A typical spectrum for the calcined 20% Fe_2O_3/SiO_2 (R10) is shown in Figure 4, spectrum b.

3.3. XRD. The XRD patterns for the 10 and 20% calcined Fe_2O_3/SiO_2 composites obtained by calcination ramp rates of 1 and 10 °C min^{-1} (indicated as R1 and R10, respectively) along with XRD pattern for the calcined blank silica (R1) are shown
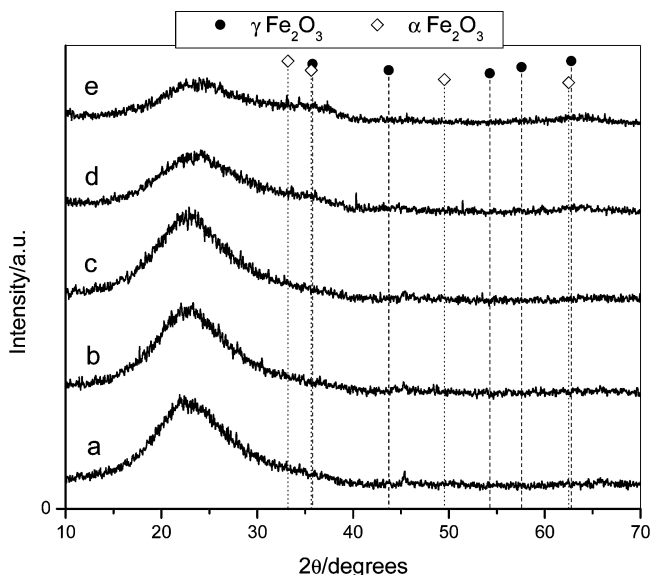
Figure 5. XRD for the calcined materials as indicated: (a) blank silica, (b) 10% Fe$_2$O$_3$/SiO$_2$ R1, (c) 20% Fe$_2$O$_3$/SiO$_2$ R1, (d) 10% Fe$_2$O$_3$/SiO$_2$ R10, and (e) 20% Fe$_2$O$_3$/SiO$_2$ R10.

in Figure 5. All the calcined composites showed amorphous patterns, and no peaks were observed in any case, no matter the ramping rate and/or the composite ratio. The question that arises here is about the case of the Fe$_2$O$_3$ phase: Is it present as a true amorphous phase, or as a case of small nanocrystalline particles below the detection size limits (5 nm) of the XRD? However, because of the absence of any line broadening at any characteristic 2θ position for crystalline Fe$_2$O$_3$ phases, and in light of the criteria that has been indicated[20] for distinguishing between these two confusing cases, it is reasonable to consider the presence of amorphous Fe$_2$O$_3$ rather than small sized nanoparticles of Fe$_2$O$_3$.

It is known that nanoparticles of amorphous Fe$_2$O$_3$ crystallize into nanocrystalline maghemite, γ-Fe$_2$O$_3$,[20] and this transformation is normally characterized by an exothermic peak at 280 °C. However, it has been reported that Fe$_2$O$_3$—SiO$_2$ amorphous nanoparticle systems show a major difference from the case of pure amorphous nanoparticles of Fe$_2$O$_3$, in spite of the fact that the same transformation phase product (i.e., γ-Fe$_2$O$_3$) was observed. The difference appears in the shifting of the transformation temperature toward higher crystallization temperature (ca. 700 °C). The shifting of the crystallization temperature toward higher temperature and the consequent stabilization of the amorphous Fe$_2$O$_3$ nanophase is attributed to what is called the preventive role of the silica matrix.[18]

3.4. Nitrogen Adsorption. Nitrogen adsorption/desorption isotherms for the 10 and 20% Fe$_2$O$_3$/SiO$_2$ composites calcined at 1 and 10 °C min^{-1} are shown in Figure 6 top and bottom, respectively. According to the original IUPAC classification,[36] the isotherms obtained with the different composites are classified as type IV isotherms with H3 type hysteresis loops. However, according to the extended classification of adsorption isotherms,[37] the isotherms are classified as type IIb isotherms. S_{BET} values obtained for the 10 and 20% composites calcined at 1 °C min^{-1} were 63.4 and 90.8 m^2 g^{-1}, respectively, as shown in Table 2, whereas, S_{BET} values for the corresponding 10 and 20% composites calcined at 10 °C min^{-1} were 62.1 and 84.5 m^2 g^{-1}, respectively, as shown in Table 2.

(36) Sing, K. S. W.; Everett, D. H.; Haul, R. A. W.; Moscou, L.; Pierotti, R. A.; Rouquerol, J.; Siemieniewska, T. *Pure Appl. Chem.* **1985**, *57*, 603.
(37) Rouquerol, F.; Rouquerol, J.; Sing, K. *Adsorption by Powders and Porous Solids*; Academic Press: London, 1999.
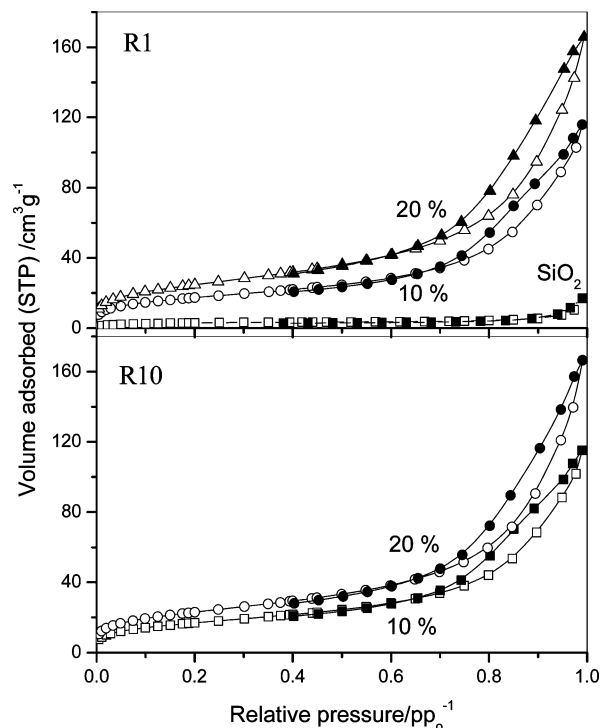

Figure 6. Nitrogen adsorption/desorption isotherms for the 10% and 20% Fe$_2$O$_3$/SiO$_2$ R1 composites along with the isotherm for the blank silica R1 material (top), and for the 10% and 20% Fe$_2$O$_3$/SiO$_2$ R10 composites (bottom).

Table 2. Textural Characteristics of the Calcined Test Materials

material	S_{BET}/ m^{2}g^{-1}	c_{BET}	t-method m^{2}g^{-1} S_t	S_{mic}	V_p/ cm^{3}g^{-1}	W_p/nm $4V_pS_{BET}^{-1}$	BJH
blank SiO$_2$ R1	10.9				0.0182	6.62	
10%Fe$_2$O$_3$/SiO$_2$ R1	63.4	88.8	58.8	4.6	0.1593	10.04	8.98
20%Fe$_2$O$_3$/SiO$_2$ R1	90.8	78.1	88.1	2.7	0.2202	9.69	8.96
10%Fe$_2$O$_3$/SiO$_2$ R10	62.1	77.7	59.3	2.8	0.1574	10.13	9.01
20%Fe$_2$O$_3$/SiO$_2$ R10	84.5	80.6	79.9	4.6	0.2159	10.22	8.98

The results indicate that the surface areas of the materials are ordered as follows: 20% composites > 10% composites > blank silica material (silica particles S_{BET} = 10.9 m^2 g^{-1}). Moreover, as shown from Table 2, higher surface areas were produced upon implementation of the lower ramp rate (1 °C min^{-1}), especially for the 20% Fe$_2$O$_3$/SiO$_2$ composite.

Further textural details, including results of t-method (S_t and S_{mic}) analysis, total pore volume V_p, and pore width W_p (via the average $4V_pS_{BET}^{-1}$ method and BJH method) were obtained and cited in Table 2. For the different test materials, the obtained S_t value was very close to the S_{BET} one, and the S_{mic} value was ≤4.6 m^2 g^{-1}, which indicates good mesoporous characteristics. Moreover, V_p values of 0.1593 and 0.2202 cm^3 g^{-1} were obtained for the 10 and 20% Fe$_2$O$_3$/SiO$_2$ (R1) calcined composites, respectively, whereas V_p values of 0.1574 and 0.2159 cm^3 g^{-1} were obtained for the 10 and 20% Fe$_2$O$_3$/SiO$_2$ (R10), respectively. Noting the total pore volume for the calcined blank silica, V_p = 0.0182 cm^3 g^{-1}, it is evident that the developed porosity was due to the composite texture formation. Moreover, the average pore width, W_p, for all of the calcined composites was about 10.00 (±0.35) nm, whereas the corresponding BJH pore width was 9.00 (±0.05) nm, as shown in Table 2.

3.5. SEM. Scanning electron micrographs for the uncalcined materials are shown in Figure 7a and b, where the characteristic spherical morphology of the silica particles can be observed.
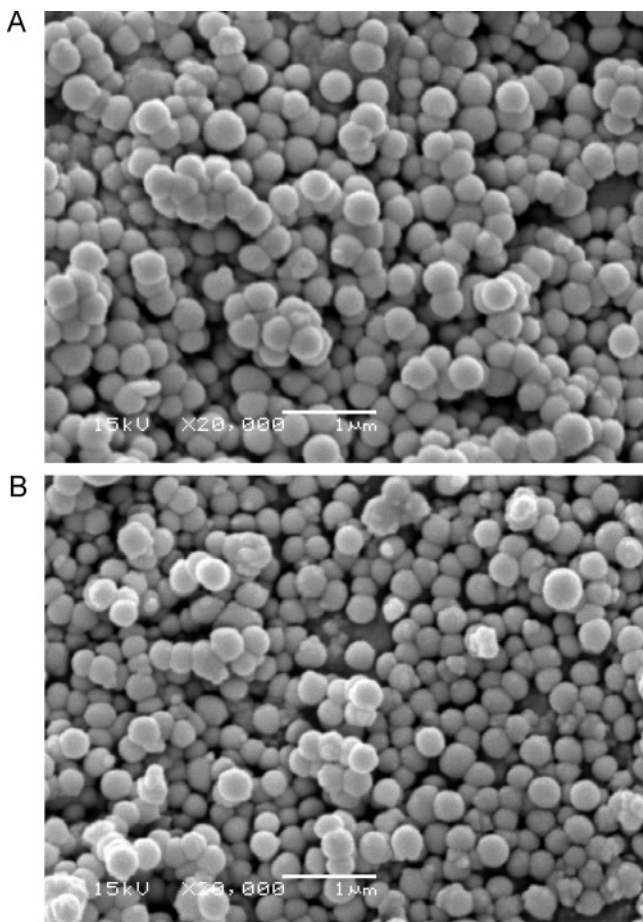
Figure 7. SEM micrographs for the uncalcined (a) 10% Fe_2O_3/SiO_2 R1, and (b) 20% Fe_2O_3/SiO_2 R1 composites.

Figure 8. SEM micrographs for the calcined (a) 10% Fe_2O_3/SiO_2 R1, and (b) 20% Fe_2O_3/SiO_2 R1 composites.

Most of the silica particles were in the range of 250−350 nm, which is the normal size and distribution in similar systems. Thus, within the silica particle matrix, aggregates of iron oxide precursor are clearly dispersed on the surface of the silica particles as a shell for the silica particles (core). However, aggregates of the iron oxide phase precursor are much more obvious for the 20% than for the 10% Fe_2O_3/SiO_2 uncalcined precursor, i.e., finer dispersion occurs for the 10% than for the 20% one.

Scanning electron micrographs for the calcined 10 and 20% Fe_2O_3/SiO_2 (R1) composites are shown in Figure 8a and b, respectively. The spherical morphology of silica particles covered by Fe_2O_3 aggregates, which was observed for the uncalcined composites, was preserved for the calcined materials. No obvious sintering of silica particles was observed, probably because of the induced roughness of the particle due to the presence of Fe_2O_3 dispersed particles and/or aggregates on the silica particle surface. For the calcined 20% composite (Figure 8b), it is observable that the shape of Fe_2O_3 aggregates was irregular, and the size was far less than 0.10 μm in diameter, whereas, smaller aggregates can be recognized for the calcined 10% composite (Figure 8a). The observed morphology is similar to that shown for Fe_2O_3/SiO_2 composites that were prepared from pre-made Stöber particles and iron pentacarbonyl ($Fe(CO)_5$).[16] However, the present method has the virtue of being direct (one pot) and utilizing ordinary precursors, namely, TEOS and $Fe(NO_3)_3 \cdot 9H_2O$.

The above results highlight the suitability of nitrate salts to prepare iron oxide nanoparticles. In this context, we should refer 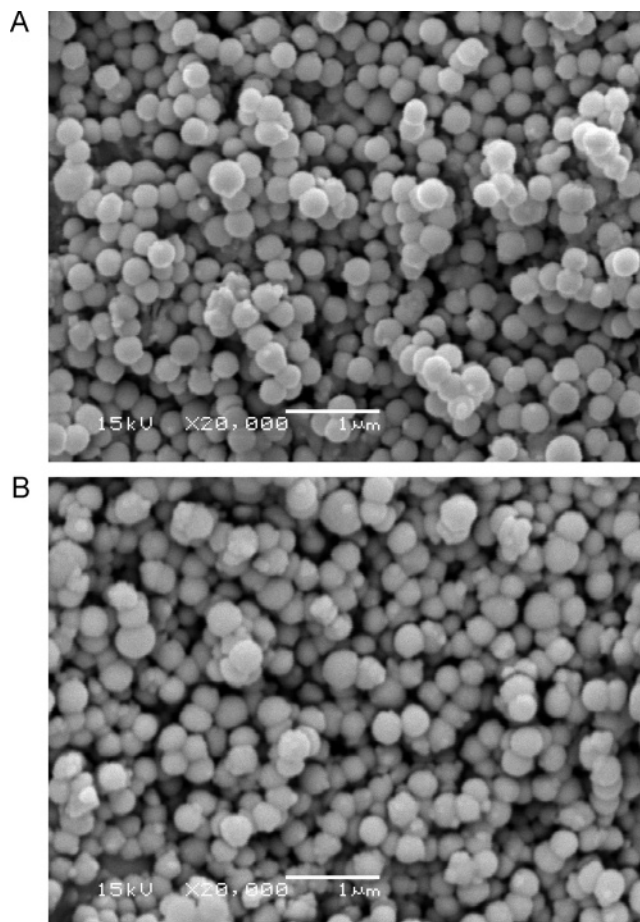to the chemistry of hydrolysis and condensation of inorganic species. Note that cations of iron (III) nitrate hydrate, when dissolved in water, are solvated by water molecules to form an aquo complex of the formula $[Fe(H_2O)_n]^{3+}$. On the basis of the water acidity and the magnitude of charge transfer,[38] the following equilibria are established for the solvated metal cations leading to hydrolysis:

$$[M(OH_2)]^{z+} \leftrightarrows [M-OH]^{(z-1)+} + H^+ \leftrightarrows [M=O]^{(z-2)+} + 2H^+$$
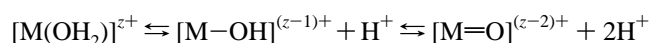
It is known that low-valent cations (z < 4), such as Fe^{3+}, yield aquo, hydroxo, or aquo−hydroxo complexes over the complete pH scale. Accordingly, at a pH value of ∼10, similar to the present preparation, aquo−hydroxo or hydroxo complexes should be expected. Condensation of the hydrolyzed species may occur through olation (a condensation process in which a hydroxyl bridge is formed) or oxolation (a condensation reaction in which an oxo bridge is formed). The addition of base to the solutions of Fe(III) nitrate precursor produces precipitate having a composition between α-FeOOH and α-Fe_2O_3.[38]

The mechanism of iron oxide phase formation from inorganic salts is composed of the following steps:[39]

(1) formation of "low molecular weight" species;

(2) further condensation to form a red cationic polymer;

(3) aging of the polymeric species leading to oxide phases; or

(38) Brinker, C. J.; Scherer, G. W. *Sol-Gel Science: The Physics and Chemistry of Sol-Gel Processing*; Academic Press: New York, 1990; pp 21−42.
(39) Flynn, C. M., Jr. *Chem. Rev.* **1984**, *84*, 31.

(4) precipitate of oxide phases directly from low molecular weight precursors.

Thus, the condensation process is very important, i.e., dimerization of $[Fe(OH)(OH_2)_5]^{2+}$ precursor produces γ-FeOOH nuclei, whereas $[Fe(OH)_2(OH_2)_4]^{1+}$ precursor condenses to form polycationic spheres 2−4 nm in diameter (each one consists of about 100 Fe(III) ions) of the composition $[Fe_4O_3(OH)_4]_n^{2n+}$. The addition of base or longer aging leads to aggregation of the latter primary particles into needles of α-FeOOH, which undergo a second-order aggregation process.

The role of the anion must be highlighted too, because it forms the counterion after dissolution of the salt in water. Anions are known to compete with aquo ligands for coordination to the metal centers and may affect the evolving particle morphology and stability.[38] Actually, an anion, *X*, may associate to the solvated Fe(III) ions forming an associated complex of the formula $[FeX(OH_2)_4]^{2+}$ or $[Fe(OH)(HX)(OH_2)_4]^{2+}$, which may dissociate or hydrolyze, respectively. Suitable behaviors of the Fe(III) associated complex result from ClO_4^-, NO_3^-, and HSO_4^- counterions. But, stability of the associated complex is also influenced by the extent of hydrolysis and the solution pH.[38] However, some anions such as HCO_3 are able to coordinate Fe^{3+} under basic conditions. Other anions such as SO_4^{2-} are able to serve as network-forming ligands in Zr^{4+} systems, whereas NO_3^- serves only as terminal groups.[38] Therefore, it could be concluded that the NO_3^- anion is a good choice because it forms a suitable Fe(III) associated complex and thereby affects the evolving particle morphology and stability.

In addition to the above conditions that encourage the formation of small nanoparticles, there is another important variable in the present method, which is the presence of the hydroxylated spherical silica particles. The latter particles act not only as a separating phase for iron oxide nanoparticles but also offer high surface area, rich with hydroxyl groups. The presence of the hydroxylated spherical silica particles, as a different separating phase, interrupts the crystallization mechanism of iron oxide and/or attracts them to their hydroxylated silica surface. Therefore, upon drying and calcination of the composite materials, and because of the small size of the iron oxide particles and/or their limited mobility, normal crystallization behavior was interrupted and thus a short ordered (amorphous) phase was produced.

Conclusions

A direct preparation method for the preparation of amorphous mesoporous Fe_2O_3/SiO_2 nanocomposites from simple precursors, namely, TEOS and $Fe(NO_3)_3\cdot9H_2O$, was described. Controlling the preparation conditions for fast nucleation and short-time growth for the iron oxide particles allows nanosized metal oxide particle formation. The method produces a thermally stabilized amorphous Fe_2O_3 phase dispersed on the surface of spherical silica particles in a somewhat shell and core morphology. The iron oxide phase was found to be dispersed as amorphous nanoparticles and/or aggregates. In spite of the fact that the pure amorphous nanoparticle phase of Fe_2O_3 is characterized by a phase transformation at a low temperature (as low as <300 °C), the present Fe_2O_3/SiO_2 composite was found to resist this transformation for up to 600 °C, at least. The present Fe_2O_3/SiO_2 composite materials offer a higher surface-to-bulk ratio and mesoporous texture for the amorphous iron oxide phase, which is expected to support many applications in catalysis, membranes, sensors, and so forth.